Supporting information for

A superior mulberry-like nanoparticle NiB binary catalyst for borohydride oxidation

Jinliang Cai[a, ‡], Caini Yi[a, ‡], Yuxin Xie[a], Ying Yang[a], Hang Yang [a], Changguo Chen[a],

*Yuping Liu[a], Danmei Yu[*a], and Xiaoyuan Zhou[*b]*

[a] School of Chemistry and Chemical Engineering, Chongqing University, Chongqing, 401331, P.R. China

[b] College of Physics, Chongqing University, Chongqing, 401331, P.R. China

[‡] **Co-first author:** Jinliang Cai, Caini Yi

Corresponding Authors

***Danmei Yu's** e-mail: yudanmei-1@163.com.

***Xiaoyuan Zhou's** e-mail: xiaoyuan2013@cqu.edu.cn**.**

Notes

The authors declare no competing financial interest.

Experimental Details

1. Materials characterization

The morphology of the prepared catalysts was characterized by scanning electron microscopy (SEM, JSM-7800F) and transmission electron microscopy (TEM, JEM 2100 F). X-ray diffraction (XRD) patterns of the prepared catalysts were obtained using a Shimadzu XRD6000 diffractometer with Cu Kα radiation in the range of diffraction angles from 30° to 90°. X-ray photoelectron spectroscopy (XPS, Thermo Fisher Scientific ESCALAB250Xi, Al Kα) analysis was performed to explore the valence and composition of elements on material surface, using C1s (binding energy (BE) of 284.8 eV) as a reference.

2. Electrochemical performance measurements

All electrochemical performance tests were performed in a three-electrode system in which the prepared catalyst was used as WE, carbon strip as CE, Hg/HgO as RE, and a mixture of 0.135 mol L^{-1} $NaBH_4$ and 2.000 mol L^{-1} NaOH as electrolyte. The activity of prepared catalysts was evaluated by linear scanning voltammetry (LSV), which was measured in the mixture solution of 0.135 mol L^{-1} $NaBH_4$ and 2.000 mol L^{-1} NaOH at a scan rate of 10 mV s^{-1}. To study the electronic transmission capability of prepared catalyst electrodes, the electrochemical impedance spectroscopy (EIS) technique was conducted at open circuit potential with potential amplitude of 5 mV and a frequency range of 0.01 Hz to 100 kHz. Fuel utilization on the catalyst was evaluated by Chronopotentiometry (CP), which was implemented at a current density of 10 mA cm^{-2} using the LAND test system. Fuel efficiency can be calculated from Eq. (1):

$$\eta = \frac{tI}{nZF} \tag{1}$$

where η stands for fuel efficiency, t is the discharge time, I is the constant current density in the discharge, n is the electron transferred number, which is 4 for Ni, Z is the amount of substance of $NaBH_4$ and F is Faraday constant (94685 C mol^{-1}).

The prepared catalyst electrodes were subjected to the accelerated durability test (ADT), which performed 500 repetitive cyclic voltammetry (CV) in the mixed solution of 0.135 mol L^{-1} $NaBH_4$ and 2.000 mol L^{-1} NaOH at a scan rate of 100 mV s^{-1} from 0 to 0.2 V *vs* RHE, to observe the change of current density before and after test thus evaluating the catalyst stability. The electron transferred number of BOR on prepared catalyst electrodes could be determined by CV method. At first the prepared catalyst was cut into a size of 3 mm × 3 mm and fixed on the surface of a rotating disc electrode (RDE, Φ=5 mm). The CV of BOR on prepared catalyst electrode was conducted at different disk rotating speeds (100, 200, 300, 400, and 500 rpm) and a scan rate of 20 mV s^{-1} in a conventional three-electrode system, in which a RDE was employed as WE, carbon rod as CE, Hg/HgO electrode as RE, and a mixture solution of 5 mmol L^{-1} $NaBH_4$ and 1 mol L^{-1} NaOH as electrolyte. The transferred electron number can be calculated according to the Koutecky-Levich equation, as follows:

$$j^{-1} = j_k^{-1} + j_d^{-1} = j_k^{-1} + B^{-1}\omega^{-0.5} \tag{2}$$

In the formula, j_k^{-1} is the dynamic current density, j_d^{-1} is the diffusion-limited current density, and ω is the rotational speed of RDE. B can be obtained based on Levich equation (Eq.3).

$$B = 0.62nD^{2/3}Fv^{-1/6}c_0 \quad (3)$$

Here, n is the transferred electron number, D is the diffusion coefficient of BH_4^- (2.6×10^{-5} cm^2 s^{-1}), F is the Faraday constant (96485 C mol^{-1}), v is the kinematic viscosity of the electrolyte (0.0118 cm^2 s^{-1}), and c_0 is the concentration of $NaBH_4$ (5 mmol L^{-1}). The value of activation energies (E_a) of BOR on the prepared catalyst electrodes were determined by the Arrhenius equation:

$$\frac{\partial \ln j}{\partial 1/T} = -\frac{E_a}{R} \quad (4)$$

where j (mA cm^{-2}) is the current density of BOR measured at E = 0.3 V *vs.* RHE, T (K) is the reaction temperature, E_a (J mol^{-1}) is the activation energy, R is the gas constant (8.314 J mol^{-1} K^{-1}).

Electrochemical active surface area (ECSA) could be identified by the double-layer capacitance test using CV method. The CV test on prepared catalyst electrode was performed in 1 mol L^{-1} KOH solution in the range of ±0.025 V open circuit potential. The ECSA of the prepared catalyst could be obtained by Eq. 5 and Eq.6:

$$i_c = vC_{DL} \quad (5)$$

$$\mathrm{ECSA} = C_{DL} / C_s \quad (6)$$

where C_s is the theoretical specific capacitance of Ni catalyst in alkaline electrolyte, which is 40 μF cm^{-2}. Moreover, all test results can be found in Table S2.

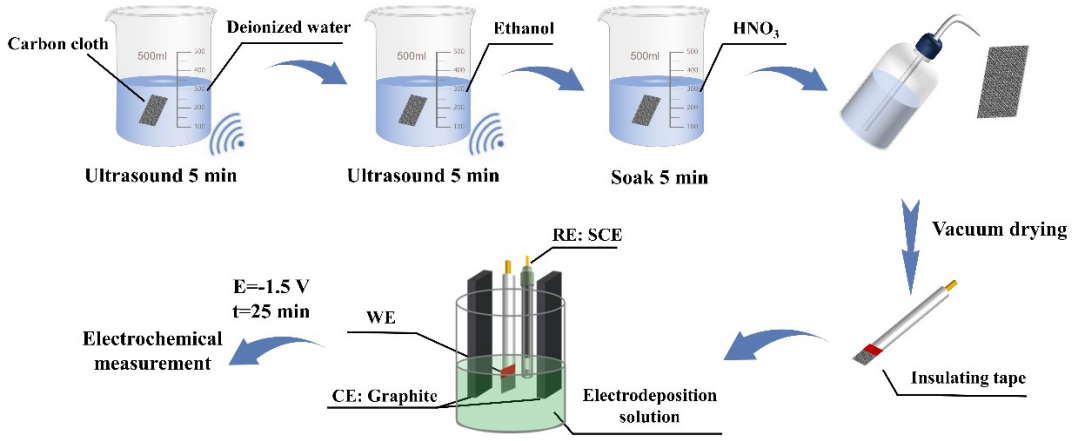

Fig. S1 Schematic diagram of catalyst preparation process

Preparation of catalyst electrodes

(1) Carbon cloth pretreatment

At first, the carbon cloth was cut into rectangles of 1 cm × 2 cm using scissors. Then it was cleaned ultrasonically in deionized water and ethanol for 5 minutes to remove any contaminants that might be contained on the surface. After that, the ethanol on the surface of carbon cloth was washed off with deionized water to avoid the violent reaction with concentrated nitric acid. And then the pretreated carbon cloth was submerged in concentrated nitric acid for 5 minutes in a fume hood, thus improving its hydrophilicity to enhance electrodeposition effect. Finally, the carbon cloth was carefully removed from HNO_3 solution and cleaned ultrasonically in deionized water for 5 minutes, then removed and dried on standby.

(2) Configuration of electrodeposition solution

Under normal temperature and pressure, 0.05 mol L^{-1} $NiCl_2 \cdot 6H_2O$, 0.5 mol L^{-1} NaCl, 0.05 mol L^{-1} $C_6H_5Na_3O_7$, 0.1 mol L^{-1} HNO_3 and H_3BO_3 were mixed to form the electrodeposition solution for the preparation of NiB catalysts. Among them, $NiCl_2 \cdot 6H_2O$ was used as the source of Ni, while H_3BO_3 was used as the source of B in

the catalyst. To promote the co-deposition of Ni and B, $C_6H_5Na_3O_7$ was acted as a ligand in the deposition solution, NaCl was employed as a conductive medium to enhance the conductivity of deposition solution. Moreover, the pH of deposition solution was adjusted by dilute nitric acid.

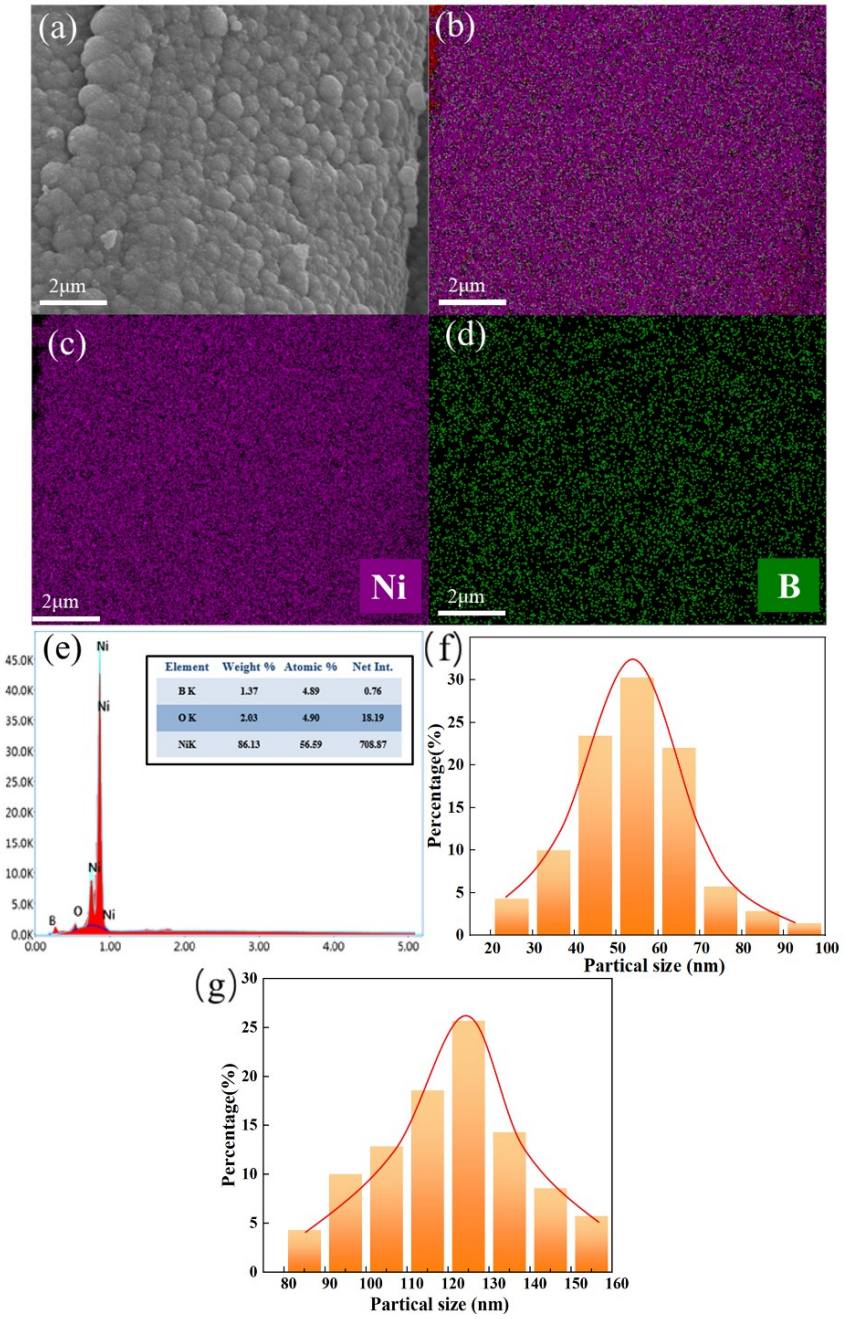

Fig. S2 (a) Local magnification SEM image of NiB-0.2, (b-d) EDS elemental distribution of NiB-0.2, (e) EDS spectrum of NiB-0.2, (f-g) Particle size distribution of NiB-0.2 and NiB-0.3 based on Fig 1(g-h).

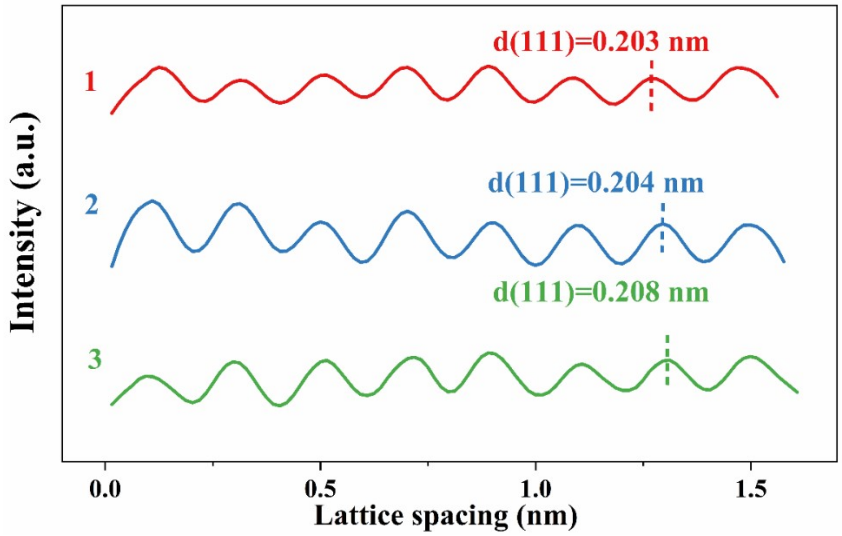

Fig. S3 Light intensity profiles of lattice fringe images in Fig. 1(k-l).

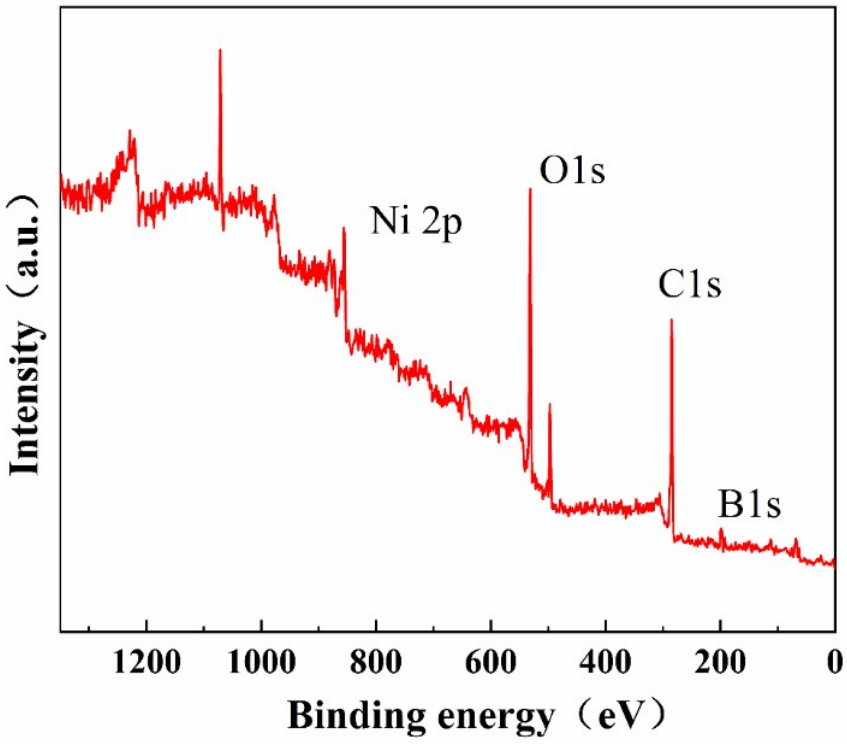

Fig. S4 XPS spectrum of survey for NiB-0.2 catalyst.

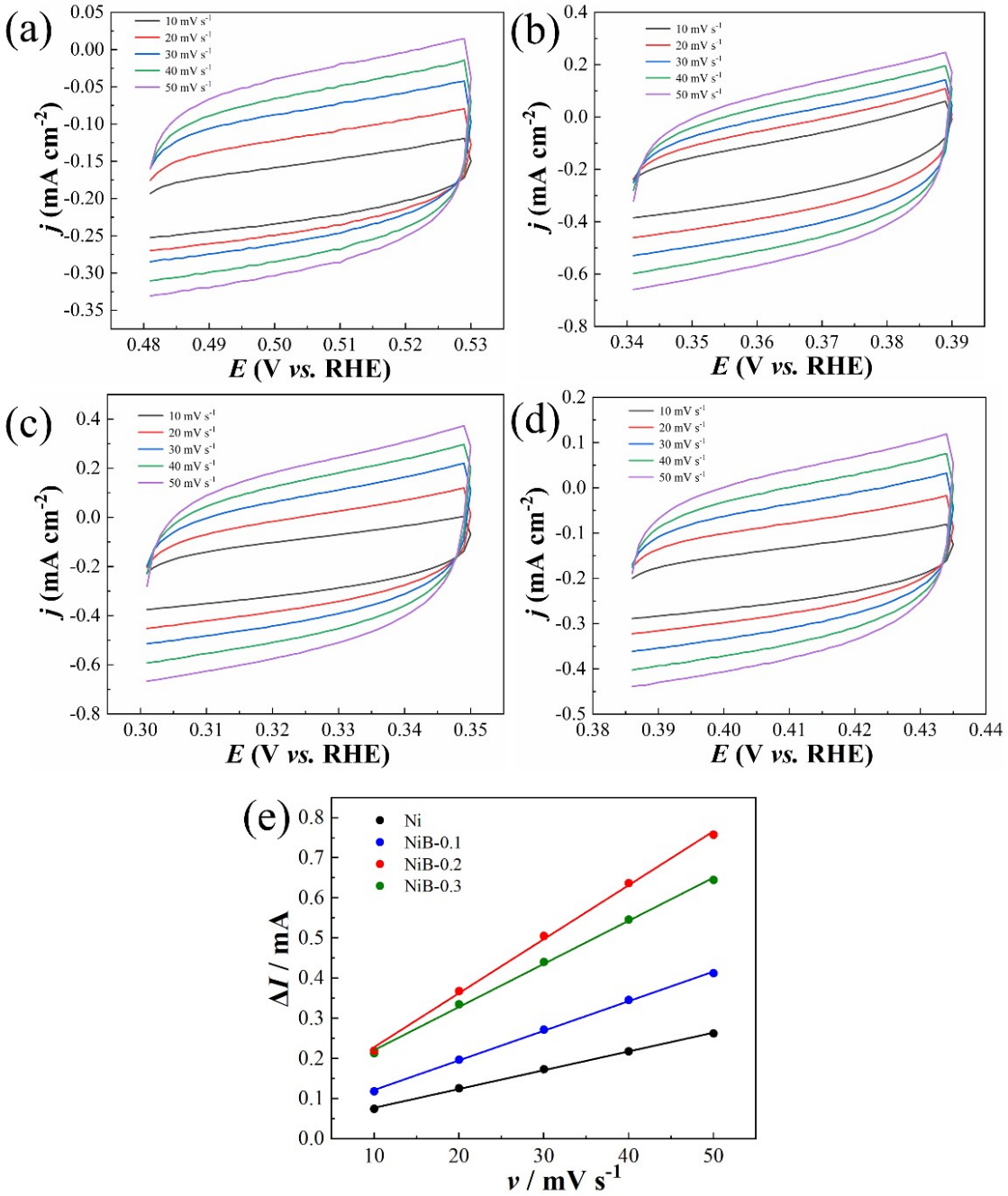

Fig. S5 The CV curves on (a) Ni, (b) NiB-0.1, (c) NiB-0.2, and (d) NiB-0.3 catalysts in 1 mol L^{-1} KOH solution; (e) $v \sim \Delta I$ fitting curves on different catalysts.

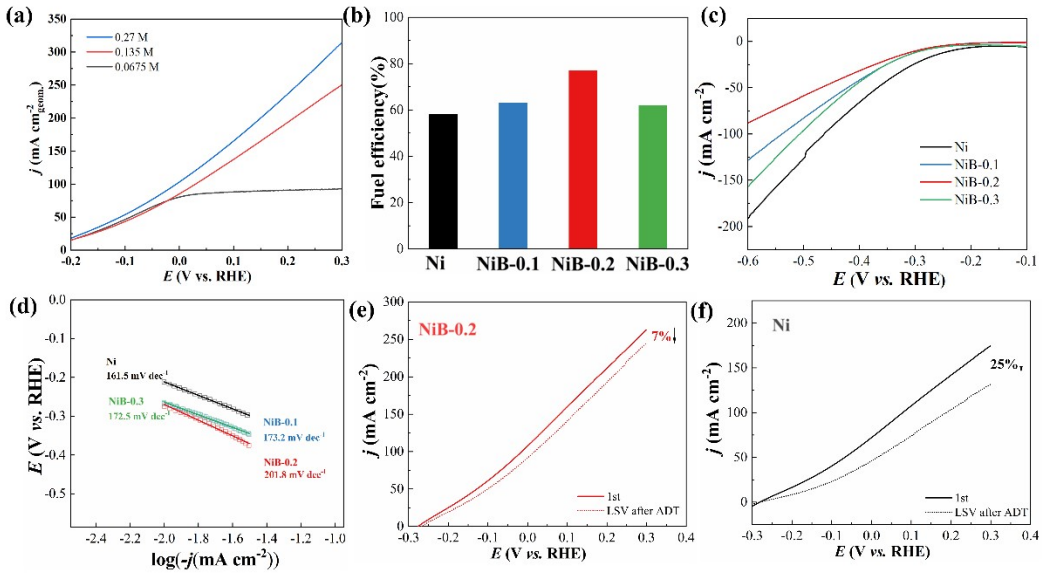

Fig. S6 (a) LSV curves of NiB-0.2 on BOR at different $NaBH_4$ concentrations; (b) Fuel effciency of BH_4^- on Ni and NiB-x; (c)LSV curve and (d) Tafel curve of HER on Ni and NiB-x; ADT curves of (e) NiB-0.2 and (f) Ni.

The LSV curves of BOR on NiB-0.2 at different concentrations of sodium borohydride have been tested, and the results are shown in the Fig. S6(a). It can be found that the current density of BOR increases with the rise of the borohydride concentration. However, the current density only increased by 25% when the concentration is double (0.27 M). This may be due to the increased concentration of borohydride leading to severe borohydride hydrolysis, thus generating more hydrogen gas, hindering liquid phase mass transfer and covering active sites. While the reduction of active sites exposed on the electrode surface can result in a low catalytic performance. [1] Therefore, considering comprehensively, the concentration of sodium borohydride is chosen 0.135 M in research electrochemistry performances.

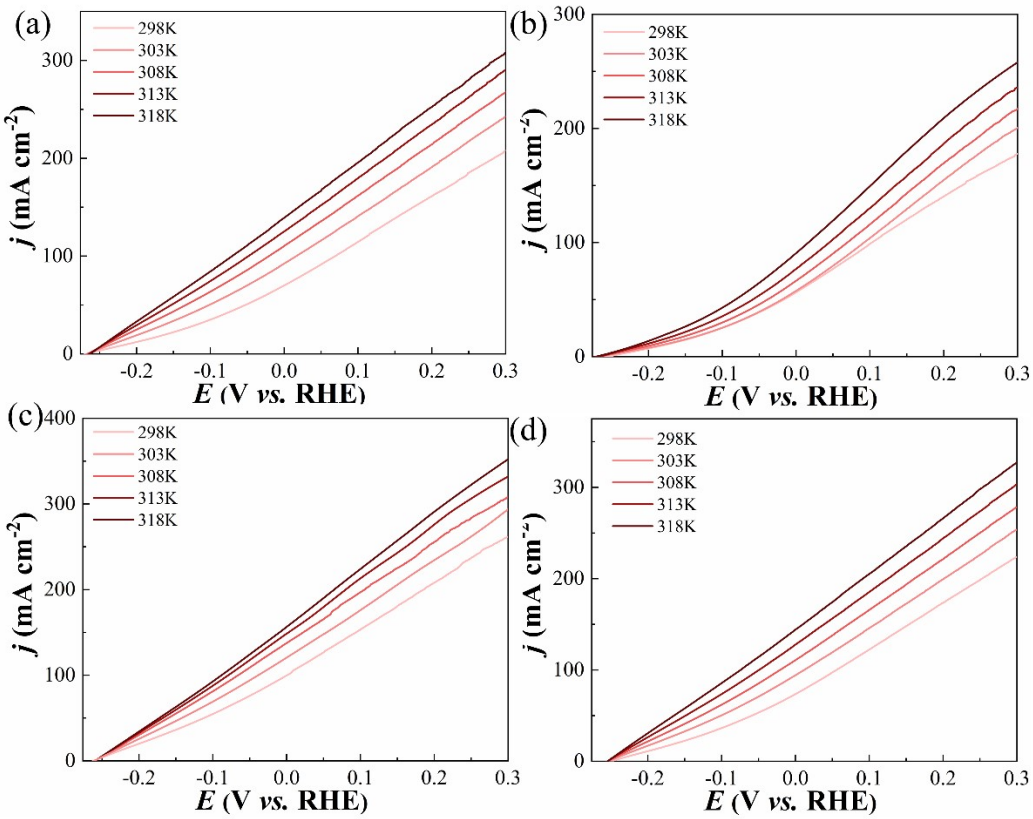

Fig. S7 CV curves of BOR in 0.135 mol L^{-1} $NaBH_4$ and 2 mol L^{-1} NaOH solutions at different temperatures on (a)Ni, (b)NiB-0.1, (c)NiB-0.2, (d)NiB-0.3.

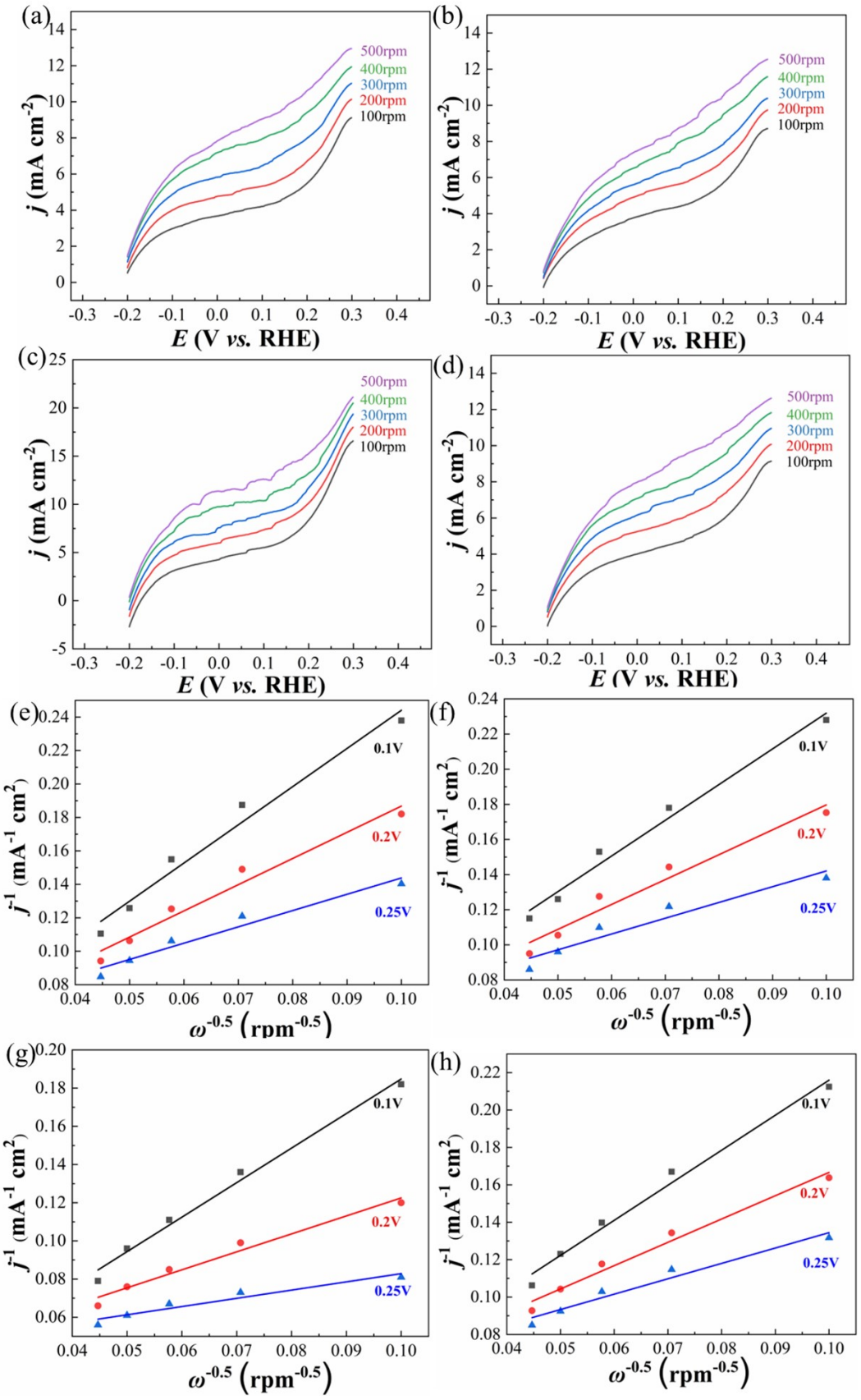

Fig. S8 CV curves of BOR on (a) Ni, (b) NiB-0.1, (c) NiB-0.2, (d) NiB-0.3; Koutecky-Levich plots on (e) Ni, (f) NiB-0.1, (g) NiB-0.2, (h) NiB-0.3.

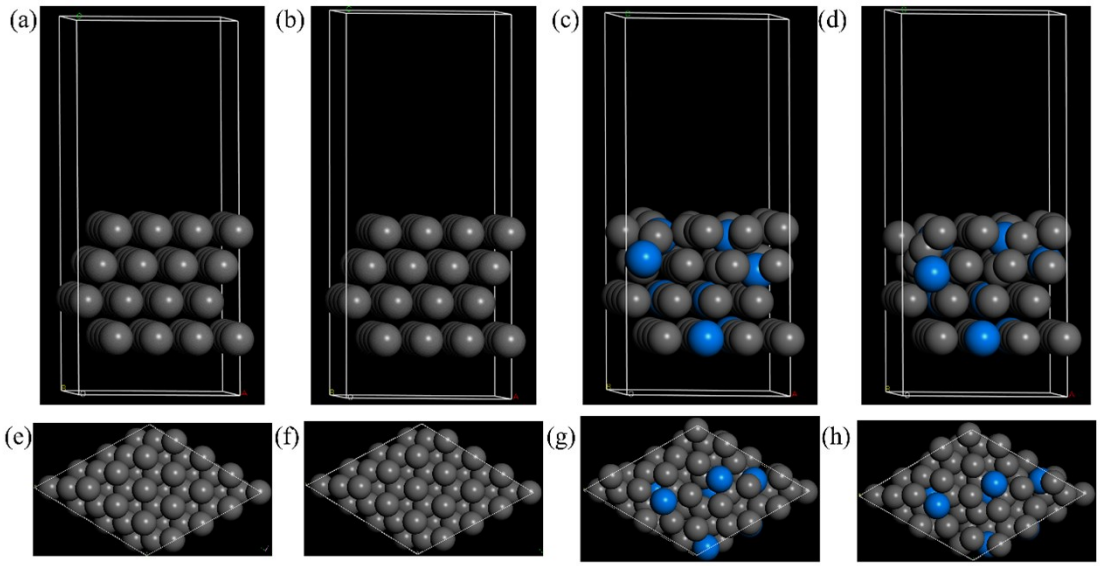

Fig. S9 Side view of the DFT calculation model for (a) Bulk Ni, (b) 2.5% strained Ni, (c) NiB-0.2, and (d) 2.5% strained NiB-0.2 and their corresponding top views (e-h).

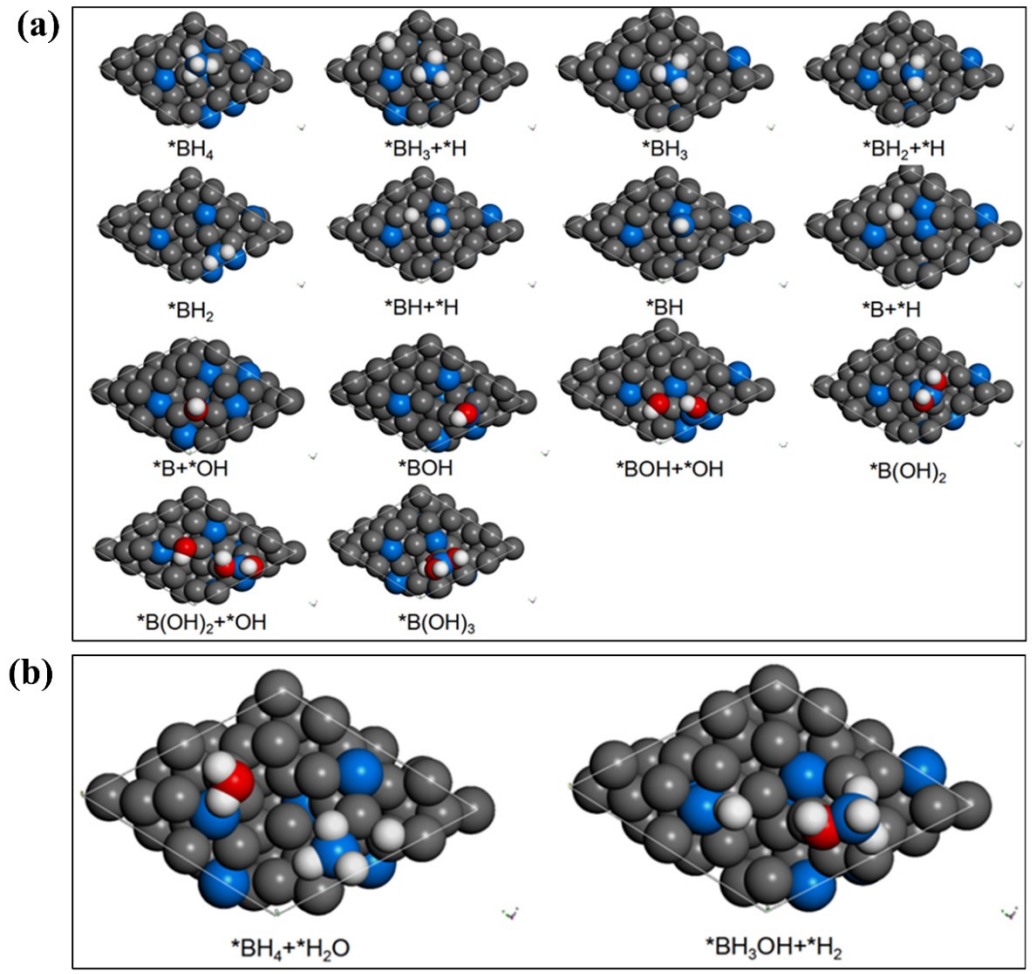

Fig. S10 DFT optimized structures of the main reaction pathways of (a) borohydride oxidation reaction and (b) borohydride hydrolysis reaction on the surface of 2.5% strained NiB-0.2. The gray, blue, red and white spheres represent Ni, B, O and H atoms, respectively.

The Vienna Ab initio Simulation Package (VASP) code was adopted to perform all spin-polarized density functional theory (DFT) calculations. [2] A 4-layer slab and 2× 2 supercells constructed with lattice bulk constants were used to represent the Ni (111) surfaces, while the ratio of B was represented by replacing Ni atoms. Moreover, a vacuum layer of ca. 15 Å was used to eliminate the interaction between periodic slabs. The generalized gradient approximation (GGA) [3] combined with Perdew–Burke–Ernzerhof (PBE) functional [4] was used. And the projector augmented wave (PAW) method [5] was employed to describe the electron–ion interactions. The plan-wave kinetic energy cut-off was 450 eV, while the 3×3×1 Monkhorst–Pack k-point mesh [6] was used to sample the Brillouin zone. In addition, the convergence criteria for the residual forces and total energies were set to be 0.01 eV /Å and 1.0×10^{-5} eV, respectively. The DFT calculation models for different catalysts established under the above conditions are displayed in Fig. S9. Besides, the DFT optimized structures of the main reaction pathways of the borohydride oxidation and hydrolysis reactions on the surface of different catalysts are also depicted in Fig. S10.

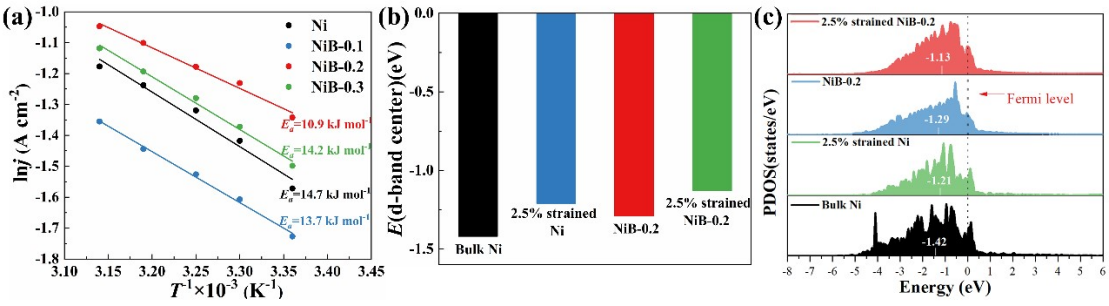

Fig. S11 (a) Arrhenius curves of BOR on different catalysts at 0.3 V, (b) d-band centres of different catalysts, (c) Density of states projected onto the 3d-orbitals of Ni atoms for different catalysts. (The Fermi level is marked by the black dashed line, and the d-band center is marked by the white solid line).

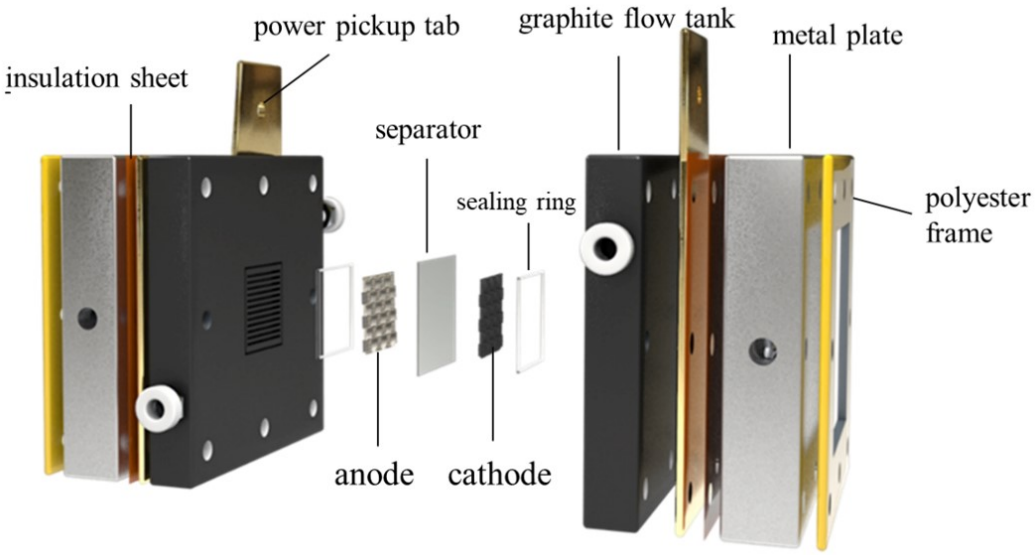

Fig. S12 Components and structure of a DBFC unit

DBFCs were assembled using the NiB-0.1, NiB-0.2, NiB-0.3, Ni or Pt/C as the anode, Pt/C as the cathode, Nafion 117 membrane as the separator, the mixed solution of 1.5 mol L^{-1} $NaBH_4$ and 3 mol L^{-1} NaOH as the anode electrolyte, and the mixed solution of 1.5 mol L^{-1} H_2O_2 and 2 mol L^{-1} H_2SO_4 as the cathode electrolyte. The anode electrolyte and cathode electrolyte were circulated by peristaltic pump at a rate of approximately 10 mL min^{-1} between the reservoirs and graphite tanks of cell, respectively. To obtain the maximum power density of the DBFC, a constant current discharge was performed in the NEWARE battery test system. The current kept rising at intervals of 80 mA from 0.1 mA. When the voltage of DBFC dropped significantly or the current could not reach to the set value, the measurement was stopped. Moreover, the current needed to be constant for 1 min each test. The constant-current discharge of the assembled DBFC was also conducted at a current density of 25 mA cm^{-2} in the NEWARE battery test system.

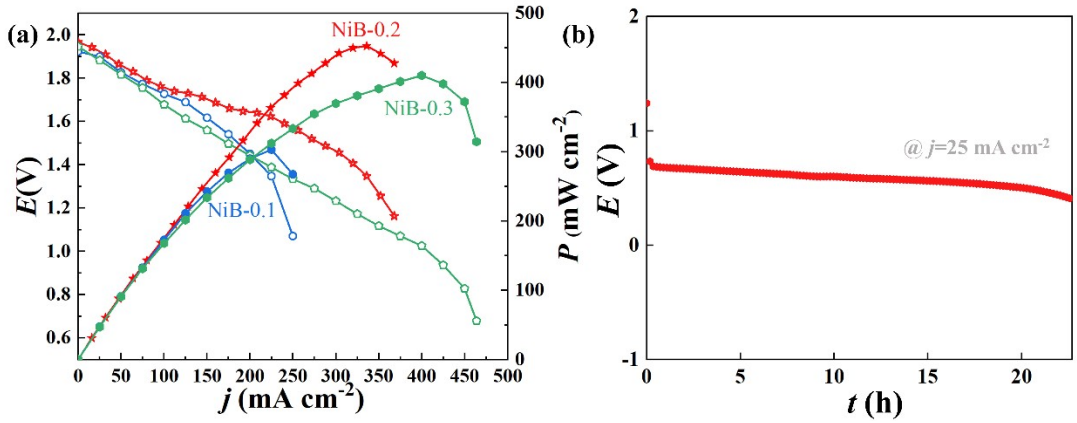

Fig. S13 (a) Polarization and power density curves of DBFCs using NiB-0.1, NiB-0.2 and NiB-0.3 anodes; (b) stability test of the DBFC with NiB-0.2 anode.

Table S1. XRD results of prepared catalysts

Catalyst	Lattice constant(Å)	Crystallite size D(nm)
Ni	3.52959	8.36046
NiB-0.1	3.54016	5.37094
NiB-0.2	3.54156	4.15816
NiB-0.3	3.54262	4.19070

The tensile stresses can be calculated by Eq.7, [7] where $a_{strained}$ is the measured lattice spacing of a certain crystal facet of prepared catalysts and a_0 is the standard lattice spacing.

$$\text{Lattice strain} = |a_{strained} - a_0| / a_0 \times 100\% \quad (7)$$

According to the calculation results, the tensile stress is 0.5% when the lattice spacing is at 2.04 Å in NiB-0.2 catalyst, while it is 2.5% when the lattice spacing reaches to a maximum of 2.08 Å. Furthermore, the tensile stress causes the elevation of the d-band center of the material, which strengthens the adsorption to the reactants. [8] So the tensile stress will affect the catalyst activity by changing the adsorption energy to the reactants or their reaction intermediate species.

Also, the D value of prepared catalysts can be calculated according to Scherrer's Eq.8 and displayed in Table S2:

$$D=K\lambda/(\beta*\cos(\theta)) \quad (8)$$

Where D is crystallite size (nm), K is the Scherrer constant (0.9), λ is the wavelength of X-ray (0.15406 nm), β is the half height width of the diffraction peak and θ is the Bragg diffraction angle. We can clearly see that the crystallite size of prepared catalysts decreases with B introduction from the calculation results.

Table S2. Summary of electrochemical performances on prepared catalysts.

Catalyst	*j*(0.3V) (mA cm^{-2})	Tafel slope (mV dec^{-1})	Rct (Ω)	ECSA (cm^{-2})	Fuel utilization (%)	Activation energy (kJ mol^{-1})
Ni	143.8	275.8	8.4	117.0	58.2	14.7
NiB-0.1	174.9	226.5	7.0	184.2	63.3	13.7
NiB-0.2	250.5	149.4	5.9	336.0	76.8	10.9
NiB-0.3	196.2	204.0	7.3	268.5	62.2	14.2

Table S3. Operating conditions of DBFC with different anode catalysts. Symbols: *T* is the operating temperature, OCV is the open circuit voltage, *P* is the power density.

Anode	Cathode	Membrane	Anolyte	Catholyte	T (K)	OCV (V)	P (mW cm^{-2})	Ref.
Ru@ Fe-BTC	Pt mesh	Nafion 117	1 M $NaBH_4$+ 4 M NaOH	5 M H_2O_2+ 1.5 M HCl	338	1.85	169	[9]
PtAu/ CNT-G	Pt/C	Nafion 115	2 M $NaBH_4$+ 6 M NaOH	2 M H_2O_2+ 1 M HCl	323	1.75	139	[10]
Pd-Ni/ N-rGO	Pt/C	Nafion 117	1 M $NaBH_4$+ 2 M NaOH	2 M H_2O_2+ 0.5 M H_2SO_4	333	2.0	353.84	[11]
Pd-Co/ N-rGO	Pt/C	Nafion 117	1 M $NaBH_4$+ 2 M NaOH	2 M H_2O_2+ 0.5 M H_2SO_4	333	1.9	275.35	[11]
Co-Ni-B	$LaNiO_3$	Polymer	0.8 M KBH_4+ 6 M KOH	O_2	298	1.06	209	[12]
PdAuNi/ C	Pt	Nafion 117	1 M $NaBH_4$+ 4 M NaOH	5 M H_2O_2+ 1.5 M HCl	348	1.9	175	[13]
NiMoN/ NC	FeN-HPC	non	1 M $NaBH_4$+ 3 M NaOH	O_2	333	2.0	112	[14]
PdCu@ rGOF	PdCu@ rGOF		0.3 M $NaBH_4$+ 2 M NaOH	1.3 M H_2O_2+ 2 M H_2SO_4	392.15		188.9	[15]
Ni@NiCu	Pt/C	Nafion 117	1.5 M $NaBH_4$+ 3 M NaOH	1.5 M H_2O_2+ 2 M H_2SO_4	343	1.94	433	[16]
Pd/ MWCNTs	$Ag_{41}Ni_{59}$/ MWCNTs	Nafion 212	5 wt% $NaBH_4$+ 10 wt% NaOH+ 85 wt% H_2O	20 wt% H_2O_2+ 5 wt% H_3PO_4+ 75 wt% H_2O	327.5± 1.5	1.68	242.8	[17]
Pd@N/C -8 foam	Pd@N/C -8 foam	Nafion 117	0.3 M $NaBH_4$+ 2 M NaOH	1.6 M H_2O_2+ 2 M H_2SO_4	333	1.73	137	[18]
NiB-0.2	**Pt/C**	**Nafion 117**	**1.5 M $NaBH_4$+ 3 M NaOH**	**1.5 M H_2O_2+ 2 M H_2SO_4**	**343**	**1.96**	**453**	**This work**

Reference

[1] D. Zhang, T. Sun, D. Cao, Y. Liu, W. Jiao, G. Wang, Journal of Power Sources 2023, **587**, 233684.

[2] G. Kresse, J. Hafner, Journal of Non-Crystalline Solids 1993, **47**, 558.

[3] G. Kresse, D. Joubert, Physical Review B 1999, **59**, 1758.

[4] (a) J. P. Perdew, K. Burke, M. Ernzerhof, Physical Review Letters 1996, **77**, 3865; (b) J. P. Perdew, A. Ruzsinszky, G. I. Csonka, O. A. Vydrov, G. E. Scuseria, L. A. Constantin, X. Zhou, K. Burke, Physical Review Letters 2008, **100**, 136406.

[5] G. G. Kresse, J. J. Furthmüller, Physical review. B, Condensed matter 1996, **54**, 11169.

[6] J. D. Pack, H. J. Monkhorst, Physical Review B 1977, **16**, 1748.

[7] T. O. He, W. C. Wang, F. L. Shi, X. L. Yang, X. Li, J. B. Wu, Y. D. Yin, M. S. Jin, *Nature* 2021, **598**, 76.

[8] F. Illas, Angewandte Chemie International Edition 2015, **54**, 10404.

[9] G. Backović, B. Šljukić, G. S. Kanberoglu, M. Yurderi, A. Bulut, M. Zahmakiran, D. M. F. Santos, International Journal of Hydrogen Energy 2020, **45**, 27056.

[10] A. Uzundurukan, E. S. Akça, Y. Budak, Y. Devrim, Renewable Energy 2021, **172**, 1351.

[11] M. G. Hosseini, V. Daneshvari-Esfahlan, S. Wolf, V. Hacker, ACS Applied Energy Materials 2021, **4**, 6025.

[12] Y.-e. Duan, S. Li, Q. Tan, Y. Chen, K. Zou, X. Dai, M. Bayati, B. B. Xu, L. Dala, T. X. Liu, International Journal of Hydrogen Energy 2021, **46**, 15471.

[13] A. M. A. ElSheikh, G. Backovic, R. C. P. Oliveira, C. A. C. Sequeira, J. McGregor, B. Sljukic, D. M. F. Santos, Nanomaterials 2021, **11**, 1441.

[14] B. He, S. Zhuang, X. Tai, J. Zhang, A. Xie, L. Cheng, P. Song, Y. Tang, Y. Chen, P. Wan, ACS Appl Mater Interfaces 2022, **14**, 17631.

[15] X. Yin, M. Hou, K. Zhu, K. Ye, J. Yan, D. Cao, D. Zhang, J. Yao, G. Wang, Renewable Energy 2022, **201**, 160.

[16] B. Hu, Y. Xie, Y. Yang, J. Meng, J. Cai, C. Chen, D. Yu, X. Zhou, Dalton Transactions 2023, **52**, 12002.

[17] S. S. Yu, T. H. Lee, T. H. Oh, Fuel 2022, **315**, 123151

[18] X. Yin, K. Zhu, K. Ye, J. Yan, D. Cao, D. Zhang, J. Yao, G. Wang, Journal of Power Sources 2022, **541**, 231704.